Power-balancing Coordinated Control of Wind Power and Demand-side Response Under Post-fault Condition

Xinshou Tian, Yongning Chi, Chao Liu, Peng Cheng, and Yan Li

***Abstract*—As the global energy transforms to renewable-based power system, the wind power generation has experienced a rapid increase. Due to the loss of synchronous machines and its frequency control mechanisms, the gradual evolution leads to critical challenges in maintaining the frequency stability. Under post-fault condition, the wind power generation has a slow recovery due to the fault ride-through (FRT) control strategy and may cause a larger frequency deviation due to the power imbalance between the supply and demand. Then, the impacts of the frequency deviations would further cause inaccuracy and instability in the control system for wind power generation. Considering the long parking time of electric vehicles (EVs), the demand-side response is provided to support the power grid via load-to-grid technology. Thus, a power-balancing coordinated control strategy of the wind power and the demand-side response is developed. It can significantly mitigate the power imbalance, thereby resulting in the enhanced frequency stability. Finally, the simulation results are provided to validate the power-balancing coordinated control strategy.**

***Index Terms*—Power-balancing, wind power, demand-side response, frequency stability, post-fault condition.**

I. Introdction

ENERGY is the material basis for supporting the human civilization. To seek for safe and clean alternative energy sources, exploring sustainable energy models has become an important part in the development trends and strategies for the energy [1], [2]. By the end of 2019, the global wind power capacity amounts to 622 GW with a 10.4% annual increase [3].

Manuscript received: December 14, 2020; revised: April 13, 2021; accepted: June 10, 2021. Date of CrossCheck: June 10, 2021. Date of online publication: September 17, 2021.

This work was supported in part by the National Natural Science Foundation of China (No. 52007174).

X. Tian (corresponding author) is with China Electric Power Research Institute, Beijing 100192, China, and he is also with North China Electric Power University, Beijing 102206, China (e-mail: xinshoutian@163.com).

Y. Chi, C. Liu, and Y. Li are with State Key Laboratory of Operation and Control of Renewable Energy & Storage Systems (China Electric Power Research Institute), Beijing 100192, China (e-mail: chiyn@epri. sgcc. com. cn; liuchao@epri.sgcc.com.cn; liyan@epri.sgcc.com.cn).

P. Cheng is with China Institute of Energy and Transportation Integrated Development, North China Electric Power University, Beijing 102206, China (e-mail: p.cheng@ncepu.edu.cn).

DOI: 10.35833/MPCE.2020.000868

With the increasing integration of wind power generation into the power system, an inevitable consequence is the loss of conventional power generation by synchronous machines and the frequency control mechanisms, which will lead to critical challenges in maintaining the frequency stability, especially under post-fault condition [4]-[6]. At the same time, the number of the electric vehicles (EVs) increases due to the potential in alleviating the environmental pollution and reducing the carbon emission [7]-[9]. Due to the long parking time and the huge stored energy, the demand-side response is provided to support the power grid with high-penetration wind power generation via various vehicle-to-grid technology. However, the converter-interfaced equipment usually operates in the grid-following mode with no frequency response capability. Thus, more efforts need to be made on maintaining the frequency stability with high-penetration wind power generation.

In recent years, several studies and practical investigations have been carried out on the frequency stability with high-penetration wind power generation. In [10]-[12], the frequency response of the power system with various generation mix, including synchronous machines and doubly-fed induction generators (DFIGs), is analyzed. Then, in order to maintain the frequency stability, several frequency-accompanying control strategies are developed and discussed, including virtual inertia control [13], [14] and primary frequency control [15]-[17]. Besides, the virtual power plant at the demand side with the vehicle-to-grid technology to support the power grid is studied [18], [19]. However, these studies are conducted under normal grid voltage conditions, which is not suitable for the grid fault conditions. Considering the grid fault, the fault ride-through (FRT) control of wind power generation is essential [20]-[22]. References [23] and [24] analyze the transient performance of the power systems during the whole process of the fault occurrence and clearance. Since the wind power has a slow power recovery under post-fault condition, the power imbalance between the supply and demand rises and continues for several seconds. Further, this will lead to the serious frequency deviation and even the disconnections of the wind power generation, which is a huge challenge for the stable operation of the power system.

Therefore, an enhanced control strategy of wind power generator, combining the FRT control and frequency response control, needs further study. Meanwhile, since the

flexibilities of EVs with the vehicle-to-grid technology are the emerging controllable sources at the demand side, it can provide the demand-side response with the additional power to support the power grid for the power balance. Thus, to maintain the frequency stability of the power grid with high-penetration wind power generation, a power-balancing strategy of the wind power and the demand-side response is proposed. Thereby, the power imbalance in the power grid can be significantly mitigated, resulting in the enhanced frequency stability.

The rest of this paper is organized as follows. In Section II, the frequency stability of the power system under post-fault condition is analyzed. The impacts on wind power are presented in Section III. Then, in Section IV, active power self-balance coordinated control strategy is presented. In Section V, the simulation study is carried out in order to validate the effectiveness of the power-balancing coordinated control. Finally, Section VI summarizes the conclusions.

II. Frequency Stability of Power System Under Post-fault Condition

A. Active Power Recovery Characteristics of Wind Power Generation Under Post-fault Condition

In order to ensure that the wind turbine does not switch off the power grid with symmetrical and asymmetrical short-circuit faults, many improved control and protection schemes are proposed in recent years. One method is to improve the resistance ability facing voltage drops by optimizing the control strategy of wind turbines. Another method is to suppress the voltage drop depth or reduce the voltage drop rate through the additional voltage support device. The decoupling control of active and reactive power is a major feature of variable-speed wind turbines. To meet the requirements of FRT capability [19], different active and reactive power control strategies can be used. The typical active power control strategy of wind turbines during the grid faults is shown in Fig. 1, where V_t is the rotor speed; $I_{\mathrm{d}}^{\mathrm{ref}}=I_{\mathrm{d}}^{\mathrm{ref,f}}+I_{\mathrm{d}}^{\mathrm{ref,s}}$ is the reference current of wind turbines during grid faults; and P_{ref} is the reference active power.

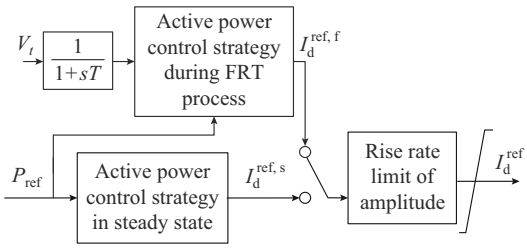

Fig. 1. Diagram of active power control strategy of wind turbines during grid faults.

The first-order inertia module simulates the process of detecting the bus voltage in Fig. 1. Generally, the FRT control of wind turbine switches is enabled when a voltage drop is detected. The wind turbines of different manufacturers have different output power characteristics according to the analysis based on the measured data of FRT, and the power of wind turbine is controllable. At the same time, all wind turbines meet the technical requirement that the active power of wind turbines returns to the pre-fault values with an active power change of at least $0.1P_{\mathrm{N}}$ under post-fault condition. Assuming that the wind speed does not change during the FRT, the active power of wind turbine under post-fault condition can be expressed as:

$$P_{\mathrm{E}}(t)=\begin{cases}0.1P_{\mathrm{N}}t & 0\le t<10,\ 0.1P_{\mathrm{N}}t<P_0\\ P_0 & 0\le t<10,\ 0.1P_{\mathrm{N}}t\ge P_0\\ P_0 & t\ge 10\end{cases} \tag{1}$$

where $P_{\mathrm{E}}(t)$ is the real-time active power; P_0 is the pre-fault active power; and P_{N} is the rated active power.

The active power of wind turbine is a time-varying variable under post-fault condition. Usually, the active power of the load in the power system is strongly related to the voltage. The electromagnetic transient process of a load can be ignored under post-fault condition, and the active power of the load is similar to instantaneous recovery. Therefore, there is a time-varying active power disturbance for the power system. The active power disturbance can be expressed as:

$$\Delta P_{\mathrm{E}}(t)=P_0-P_{\mathrm{E}}(t)=\begin{cases}P_0-0.1P_{\mathrm{N}}t & 0\le t<10,\ 0.1P_{\mathrm{N}}t<P_0\\ 0 & 0\le t<10,\ 0.1P_{\mathrm{N}}t\ge P_0\\ 0 & t\ge 10\end{cases} \tag{2}$$

As a result, under post-fault condition, the power provision by the wind power generation has an evident decrease and a slow recovery. This would lead to the power imbalance between the generation side and the demand side for a duration of several seconds. Since the power system is unable to provide the sufficient power to meet the requirement at the demand side, there will be an obvious drop in the system frequency. Such frequency disturbance makes negative impacts on the wind power generation and even causes the disconnection of wind power generation, which may cause a larger frequency drop in the power system.

B. Frequency Performance

During the grid fault, the virtual inertia control strategy and the primary frequency control strategy of wind turbines will be inactivated. The active power recovery of wind turbines will be determined by the FRT control strategy. The equivalent inertia time constant of power system with the high-penetration wind power generation can be represented using equivalent inertia time constant H_{Σ}. In addition, the regulation of the turbine-governor equivalent model $h_{\mathrm{mT}}(s)$ and the hydraulic turbine-governor equivalent model $h_{\mathrm{mH}}(s)$ are also included. Therefore, the modified system frequency response (SFR) model shown in Fig. 2 is proposed, which includes H_{Σ}.

In the power system, the wind power generator cannot provide the inertia support and the frequency response under post-fault condition. H_{Σ} is mainly determined by the synchronous machines, which is expressed as:

$$H_{\Sigma}=\frac{\sum_{i=1}^{m}H_{\mathrm{N}i}S_{\mathrm{N}i}}{\sum_{i=1}^{n}S_{\mathrm{WF}i}+\sum_{i=1}^{m}S_{\mathrm{N}i}} \tag{3}$$

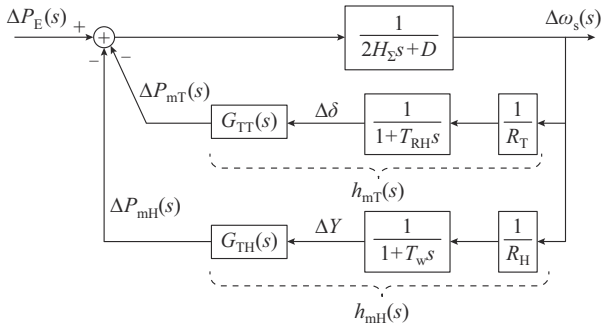

Fig. 2. Diagram of modified SFR model.

where m and n are the numbers of the synchronous machines and wind power generators, respectively; S_{Ni} and S_{WFi} are the rated capacities of the synchronous machines and wind power generators, respectively; and H_{Ni} is the inertia time of the synchronous machines.

For other power generation units without inertia support capacity, the conventional inertia time constant assessment method can also be used under such case with no inertia supporting generation such as wind power generation and solar power generation.

Taking the reheat thermal power unit as an example, the steam chamber time constant T_{CH} is much smaller than the reheater time constant T_{RH}. The dynamic response of the governor is much faster. Therefore, the dynamic response process of the governor can be ignored. In the this paper, the system frequency increment $\Delta\omega_s(s)$ is regarded as the input, while the mechanical power increment $\Delta P_{mT}(s)$ is used as the output. By this means, a simplified model of the steam turbine-governor for a single thermal power unit can be obtained. If there are multiple thermal power units, the equivalent turbine-governor aggregation model can be obtained using weighted dynamic equivalent parameter aggregation method. Thus, the system transfer function of the synchronous machines between the power imbalance and frequency deviation is given as:

$$h_{mT}(s)=\frac{\Delta P_{mT}(s)}{\Delta\omega_s(s)}=\frac{1+F_{HP}T_{RH}s}{R_T(1+T_{RH}s)} \tag{4}$$

where R_T is the adjustment coefficient of equivalent thermal power unit; T_{RH} is the reheater time constant; and F_{HP} is the aggregation parameter.

For hydropower units, the mechanical power increment $\Delta P_{mH}(s)$ can be set as the output and the system frequency increment $\Delta\omega_s$ can be also used as the input. A simplified model of a single hydropower unit can be obtained. When there are multiple hydropower units, the aggregate model of equivalent turbine-governor can be obtained using weighted dynamic equivalent parameter aggregation method. Consequently, the transfer function of the hydropower unit is:

$$h_{mH}(s)=\frac{\Delta P_{mH}}{\Delta\omega_s(s)}=\frac{1-T_w s}{R_H(1+0.5T_w s)} \tag{5}$$

where R_H is the adjustment coefficient of equivalent hydropower unit; and T_w is the aggregation parameters of water hammer effect coefficient.

For other power generation units without primary frequency control function, the calculation method of the adjustment coefficient of power system is equivalent to the power system including wind power generation. For the power generation units with primary frequency control function, the calculation method of the adjustment coefficient of power system is equivalent to the power system including synchronous generator such as nuclear power plant.

The modified SFR model describes a closed loop system, where the input variable $\Delta P_E(s)$ is the system active power shortage; the output variable $\Delta\omega_s(s)$ is the system frequency increment; the comprehensive model of system inertial response and load damping is the open-loop transfer function $G_1(s)$; and $h_{mT}(s)$ and $h_{mH}(s)$ are made up of the feedback transfer function $h_1(s)$. Therefore, when the active power recovery characteristics of wind turbine are considered under post-fault condition, a diagram of simplified transfer function with wind power change is shown in Fig. 3.

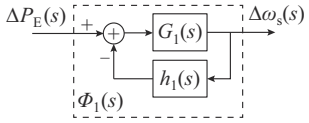

Fig. 3. Diagram of simplified transfer function with wind power change.

According to (3), the forward open-loop transfer function $G_1(s)$ in Fig. 3 can be given as:

$$G_1(s)=\frac{1}{2H_\Sigma s+D} \tag{6}$$

where D is the load damping coefficient.

In Fig. 3, considering the synchronous machines and the hydropower units, based on (4) and (5), the feedback transfer function h_1(s) can be expressed as:

$$h_1(s)=h_{mT}(s)+h_{mH}(s)=\frac{1+F_{HP}T_{RH}s}{R_T(1+T_{RH}s)}+\frac{1-T_w s}{R_H(1+0.5T_w s)} \tag{7}$$

Thus, the entire transfer function of the power system during the wind power change is presented as:

$$\Phi_1(s)=\frac{\Delta\omega_s(s)}{\Delta P_E(s)}=\frac{b_2s^2+b_1s+b_0}{a_3s^3+a_2s^2+a_1s+a_0} \tag{8}$$

$$\begin{cases} a_0=R_TR_HD+R_H+R_T \\ a_1=R_TR_H(2H_\Sigma+DT_{RH}+0.5DT_w)+ \\ \quad R_H(F_{HP}T_{RH}+0.5T_w)+R_T(-T_w+T_{RH}) \\ a_2=R_TR_H(2H_\Sigma T_{RH}+H_\Sigma T_w+0.5DT_{RH}T_w)+ \\ \quad 0.5R_HF_{HP}T_{RH}T_w-R_TT_wT_{RH} \\ a_3=R_TR_HH_\Sigma T_{RH}T_w \end{cases} \tag{9}$$

$$\begin{cases} b_0=R_TR_H \\ b_1=R_TR_H(T_{RH}+0.5T_w) \\ b_2=0.5R_TR_HT_{RH}T_w \end{cases} \tag{10}$$

Assuming that there are real poles and conjugate complex poles, the response of $\Delta\omega_s(s)$ with high-penetration wind power generation under post-fault condition is:

$$\Delta\omega_s(s)=\frac{b_2s^2+b_1s+b_0}{a_3s^3+a_2s^2+a_1s+a_0}\Delta P_E(s)=$$
$$\frac{A_0}{s}+\frac{A_1}{s^2}+\frac{A_2}{s-p_1}+\frac{B(s+\alpha\beta)+C\beta\sqrt{1-\alpha^2}}{s^2+2\alpha\beta s+\beta^2} \quad (11)$$

where A_i ($i=0, 1, 2$) is the remainder array of partial fraction expansion; p_1 is the pole array of partial fraction expansion; A_0 is the residue of $\Delta\omega_s(s)$ based on $s=0$; A_1 is the residue of $s\Delta\omega_s(s)$ based on $s=0$; A_2 is the residue of $\Delta\omega_s(s)$ based on $s=p_1$; B and C are the real and imaginary parts of the residue of $\Delta\omega_s(s)$ at the conjugate complex pole $s=-(B\pm jC)$, respectively; α is the damping coefficient of the second-order system based on the conjugate complex; and β is the oscillation angular frequency of the second-order system based on the conjugate complex.

$\Delta P_{E1}(s)$ is the power response with the wind power recovery under post-fault condition and can be expressed as:

$$\Delta P_{E1}(s)=\frac{1}{s^2}(P_0s-0.1P_N) \quad (12)$$

Accordingly, considering the power recovery of the wind power generation under post-fault condition, the frequency response of the power system in the time domain is given as:

$$\Delta f(t)=\frac{1}{2\pi}\left(A_0+A_1t+A_2e^{p_1t}+Be^{-\alpha\beta t}\cos(\beta\sqrt{1-\alpha^2}\,t)+Ce^{-\alpha\beta t}\sin(\beta\sqrt{1-\alpha^2}\,t)\right) \quad (13)$$

As can be observed, it needs a time period for the wind power generation back to the commanded active power under post-fault condition. This would lead to the power imbalance and further cause the frequency deviations. The frequency deviations are proportional to the imbalanced active power. The loads of demand-side response are normally highly dispersed, and in a small-scale power systems, the optimized control strategy is easy to achieve real-time power balance.

III. Impacts on Wind Power Generation

The frequency disturbance would decrease the accuracy of the phase-locked loop (PLL) and may lead to negative impacts on the stability of the power converter. Taking the widely-used DFIG-based wind power generation as an example, the frequency disturbance would not only reduce the accuracy of the tracking performance in the control loop, but also reduce the power provision due to the change of the rotor slip.

To ensure the grid synchronization, PLL is widely used in the control system of the asynchronous power sources. The PLL is a closed-loop dynamic system, automatically tracking the frequency and phase signal. The basic function of a PLL is to detect and output the frequency and phase angle of the input signals. To obtain the grid frequency and its phase angle, the grid voltage is used as its input. Then, the performance of the control system will change in the process of the frequency disturbance.

The structure of a typical PLL used in power electronics is shown in Fig. 4, where u_{sa}, u_{sb}, u_{sc}, u_{sd}, and u_{sq} are the switch voltages for the *abc* and *dq* frames, respectively. The loop filter $LF(s)$ is proportional plus integral controller, and $LF(s)=k_p+k_i/s$, where k_p and k_i are the proportional and integral gains, respectively.

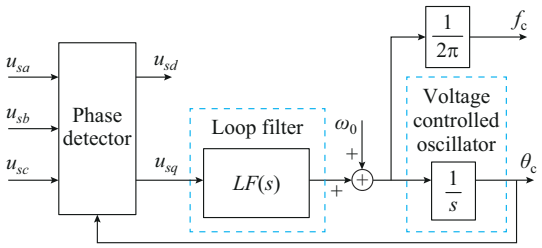

Fig. 4. Structure of a typical PLL.

According to the structure of a typical PLL shown in Fig. 4, the transfer function of the detected frequency, output by the PLL, is calculated as:

$$G(s)=\frac{f_c(s)}{\theta_c(s)}=\frac{s(k_ps+k_i)}{s^2+k_ps+k_i}=\frac{2\zeta\omega_cs^2+\omega_c^2s}{s^2+2\zeta\omega_cs+\omega_c^2} \quad (14)$$

where ω_c and ζ are the natural frequency and the damping factor, respectively, which are given as in (15).

$$\begin{cases}\omega_c=\sqrt{k_i}\\ \zeta=\dfrac{k_p}{2\sqrt{k_i}}\end{cases} \quad (15)$$

Based on the previous analysis, it is noted that the rate of change of frequency (ROCOF) is approximately equal to a constant in a determined system. Thus, the input in frequency domain of PLL can be expressed as $\Delta\varphi(s)=1/s^3$. The response of PLL under active power disturbance is obtained as:

$$\Delta f_c(s)=\frac{1}{s^3}G(s)=\frac{2\zeta\omega_cs+\omega_c^2}{s^2(s^2+2\zeta\omega_cs+\omega_c^2)} \quad (16)$$

Considering the solution complexity of (16), the response of the PLL based on different damping factors in frequency domain can be expressed as (17). Based on the inverse Laplace transform theory, the dynamic response of the PLL in the time domain can be expressed as (18).

$$\Delta f_c(s)=\begin{cases}\dfrac{1}{s^2}+\dfrac{-\dfrac{\sqrt{\zeta^2-1}}{2\omega_c(\zeta^2-1)}}{s-\left(-\zeta\omega_c+\omega_c\sqrt{\zeta^2-1}\right)}+\dfrac{\dfrac{\sqrt{\zeta^2-1}}{2\omega_c(\zeta^2-1)}}{s+\zeta\omega_c+\omega_c\sqrt{\zeta^2-1}} & 0<\zeta<1\\ \dfrac{1}{s^2}-\dfrac{1}{(s+\omega_c)^2} & \zeta=1\\ \dfrac{1}{s^2}+\dfrac{-\dfrac{\sqrt{\zeta^2-1}}{2\omega_c(\zeta^2-1)}}{s-\left(-\zeta\omega_c+\omega_c\sqrt{\zeta^2-1}\right)}+\dfrac{\dfrac{\sqrt{\zeta^2-1}}{2\omega_c(\zeta^2-1)}}{s+\zeta\omega_c+\omega_c\sqrt{\zeta^2-1}} & \zeta>1\end{cases} \quad (17)$$

$$\Delta f_c(t)=\begin{cases} t-\dfrac{\sqrt{1-\zeta^2}}{\omega_c(1-\zeta^2)}\sin\left(\omega_c t\sqrt{1-\zeta^2}\right) & 0<\zeta<1 \\ t-te^{-\omega_c t} & \zeta=1 \\ t-\dfrac{\sqrt{\zeta^2-1}}{2\omega_c(\zeta^2-1)}e^{-\left(\zeta-\sqrt{\zeta^2-1}\right)\omega_c t}+\dfrac{\sqrt{\zeta^2-1}}{2\omega_c(\zeta^2-1)}e^{-\left(\zeta+\sqrt{\zeta^2-1}\right)\omega_c t} & \zeta>1 \end{cases} \tag{18}$$

Based on the previous analysis, Fig. 5 shows the response of the PLL with different natural frequencies and damping factors under the frequency disturbance. As can be seen, the higher natural frequency and smaller damping factor, the faster response speed and the bigger overshoot. However, there may be a small oscillation amplitude. The PLL has a strong ability to track frequency change signals, and the tracking errors are small with different parameters. The maximum tracking error is about 0.8%.

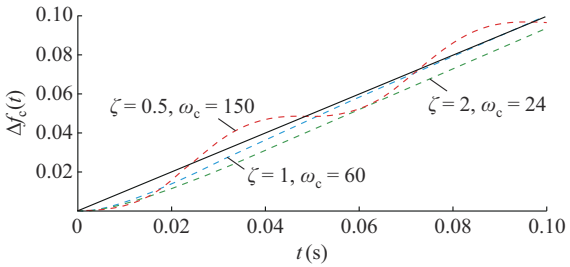

Fig. 5. Response of PLL with different natural frequencies and damping factors under frequency disturbance.

Meanwhile, the frequency deviation mainly affects the stability of DFIG-based variable-speed wind turbine. The frequency deviation will change the slip rate of DFIG, and the active power and active current flowing through the RSC will change. In a word, the frequency disturbance will have the impacts on the power provision due to the change of the rotor slip. Then, the slip active power of the rotor side converter (RSC) is given as:

$$P_r=\omega_{slip}P_E \tag{19}$$

where P_r and P_E are the rotor active power and the electromagnetic power, respectively; and the rotor slip ω_{slip} is given as:

$$\omega_{slip}=\frac{\omega_r-2\pi f_0}{2\pi f_0} \tag{20}$$

where f_0 is the actual frequency; and ω_r is the rotor angular frequency.

For a two-pair DFIG with the synchronous speed of 1500 rad/min, its rotor speed is generally 1200-1800 rad/min under normal conditions and the corresponding rotor electrical frequency is 40-60 Hz. The rotor slip of DFIG running at rated power is $\omega_{slip}\in(-20\%,+20\%)$. Based on (19), the active power of the RSC is between $-0.2P_N$ and $0.2P_N$. Considering the frequency disturbance, the maximum power delivered by the RSC is given as:

$$P_r^{\max}=\begin{cases} \dfrac{40-(f_0+\Delta f_M)}{f_0+\Delta f_M}P_N & f_0\geq 50 \\ \dfrac{60-(f_0+\Delta f_M)}{f_0+\Delta f_M}P_N & f_0<50 \end{cases} \tag{21}$$

where Δf_M is the maximum measurement error of system frequency.

According to (21), the impacts of frequency disturbance on DFIG are shown in Table I.

TABLE I
IMPACTS OF FREQUENCY DISTURBANCE ON DFIG

Frequency (Hz)	Without considering measurement error		Considering measurement error as 0.8%	
	The maximum rotor slip (%)	The maximum active power of RSC	The maximum rotor slip (%)	The maximum active power of RSC
53	–24.5	$0.245P_N$	–25.1	$0.251P_N$
52	–23.1	$0.231P_N$	–23.7	$0.237P_N$
51	–21.6	$0.216P_N$	–22.2	$0.222P_N$
50	20.0	$0.200P_N$	20.0	$0.200P_N$
49	22.4	$0.224P_N$	23.4	$0.234P_N$
48	25.0	$0.250P_N$	26.1	$0.261P_N$
47	27.7	$0.277P_N$	29.1	$0.291P_N$

As can be observed from Table I, when there is a system frequency disturbance, the maximum rotor slip and the active power of the maximum rotor slip of DFIG change significantly. For the same frequency deviation, the rotor slip and power provision are relatively larger when the system frequency decreases comparing with the increasing system frequency. When the system frequency drops to 47.0 Hz, the maximum rotor slip is 27.7%, and the active power of the maximum rotor slip is $0.277P_N$. If the measurement error of frequency deviation is considered to be 0.8%, and the actual frequency drops to 47.0 Hz, the maximum rotor slip is 29.1%, and the active power of the maximum rotor slip is $0.291P_N$. The active power of the maximum rotor slip is usually $0.2P_N$ under normal conditions. Therefore, the active power of the rotor slip may exceed the overcurrent capability of RSC and GSC with frequency deviation disturbance. Thus, an enhanced control strategy of the power system with the integration of wind power generation is essential to avoid larger frequency deviation.

IV. ACTIVE POWER SELF-BALANCE COORDINATED CONTROL STRATEGY

As analyzed previously, the slow power recovery of the wind power generation under post-fault condition would make negative impacts on the frequency of the power system with high-penetration wind power generation. The frequency disturbance would not only lead to the inaccuracy of the PLL in the control system, but also change the rotor power provision in the power flow. Then, the demand-side response to support the power grid can provide the chance to rapidly regulate the power provision against the slow active power recovery of the wind power generation.

A. Modeling on Demand-side Response

Taking EVs as an example, they can be controlled as a demand-side response, where the coordinated charging can be achieved. The advantages of EVs can be fully utilized through reasonable charging and discharging control, which can realize favorable regulation of the power grid, and improve the consumption of renewable energy and the stability of grid-connected power system. The active power balance of the power system and its influence on frequency stability within 10 s under post-fault condition are considered in the paper. The impact of the dynamic characteristics of EVs is relatively small during the transient process, where only the charging and discharging of the single EV unit are controlled.

When the following voltage constraint (22) and status constraint (23) are met, EVs are able to participate in the demand-side response control.

$$U_{\min} \le U_i(t) \le U_{\max} \tag{22}$$

where $U_i(t)$ is the connection point voltage of the i^{th} EV; $U_{\min}$ is the lower limit of voltage; and $U_{\max}$ is the upper limit of voltage.

$$\begin{cases} -P_{\text{ch,max}} \le P_{\text{ch}}(t) \le P_{\text{ch,max}} \\ S_{\text{soc,min}} \le S_{\text{soc}}(t) \le S_{\text{soc,max}} \end{cases} \tag{23}$$

where $P_{\text{ch}}(t)$ is the charging power; $P_{\text{ch,max}}$ is the upper limit of charging power; $S_{\text{soc}}(t)$ is the state of charge of battery; $S_{\text{soc,max}}$ and $S_{\text{soc,min}}$ are the upper and lower limits of the state of charge of the battery, respectively.

Assuming there are m controllable load units, the maximum controllable active power of the demand-side response $P_{\max}$ can be given as:

$$P_{\max} = \sum_{i=1}^{m} P_{\text{ch,i}}(t) \tag{24}$$

where $P_{\text{ch,i}}(t)$ is the charging power of the i^{th} EV.

B. Power-balancing Coordinated Control of Wind Power Generation and Demand-side Response Under Post-fault Condition

Consequently, a power-balancing coordinated control of wind power and demand-side response under post-fault condition is developed based on the above analysis.

Figure 6 presents the active power recovery of both wind power and demand-side response. Firstly, the active power recovery characteristics of wind power generation need to be investigated with a quantified description. Secondly, the power provision of the demand side needs to be evaluated, which is regulated based on the active power recovery of the wind power generation under post-fault condition. By means of coordinating the wind power generation and the demand-side response, the required active power can be rapidly compensated to achieve the power-balancing operation of the high-penetration wind power generation integrated into power system with enhanced frequency stability.

The implementation of the power-balancing coordinated control of the wind power generation and the demand-side response can be summarized as follows.

Step 1: determine the power grid data including the number of wind turbines, the active power of wind turbines and the maximum active power of the demand-side response.

Step 2: according to the FRT test data of the wind power generation, evaluate the active power recovery characteristics of wind power generation under post-fault condition. Determine the active power difference ΔP_{W0} between the active power in the steady state and the active power recovery of initial value of the wind power generation. Determine the active power recovery time $t_0 \le 10$.

Step 3: evaluate $P_{\max}$ of the demand-side response and the minimum controllable active power.

Step 4: judge the relationship between ΔP_{W0} and $P_{\max}$.

Step 5: if $P_{\max}$ is larger than ΔP_{W0}, the demand-side responses can be divided into n groups. The active power of group 1 is $P_1 = P_{\max} - (n-1)\Delta P_{\text{W0}}/n$; the active power of other groups is $P_i = \Delta P_{\text{W0}}/n$. The time interval of each group switching to the power grid is t_0/n.

Step 6: if $P_{\max}$ is smaller than ΔP_{W0}, the demand sides can be divided into n groups. The active power of every group is $P_i = P_{\max}/n$. The time interval of each group switching to the power grid is t_0/n. The number n of the demand-side groups based on the impact of the single active power disturbance on the system frequency is provided.

Step 7: the active power recovery of both the wind power generation and the demand-side response is given in Fig. 6.

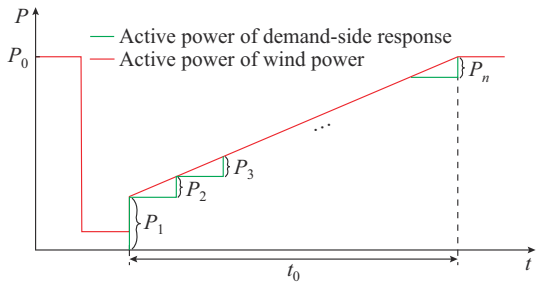

Fig. 6. Active power recovery of both wind power and demand-side response.

The demand-side response control is designed offline, and the proposed power-balancing coordinated control is activated online based on the steady-state active power and active power recovery of the wind power generation under post-fault condition, so the requirements for the communication are relatively low.

C. Stability Analysis of Power System Under Power-balancing Coordinated Control

According to the analysis in Section II, the frequency stability depends on the system active power shortage under disturbances in a certain system structure. The proposed power-balancing coordinated control strategy optimizes the active power shortage by controlling active power of wind power generation and demand-side response under post-fault condition, and the frequency stability margin can be greatly improved. The active power difference of power system under post-fault condition can be calculated as:

$$\Delta P_{\text{E}} = \Delta P_{\text{W}} - \Delta P_{\text{dr}} \tag{25}$$

where ΔP_{W} is the power difference between the active power in the steady state and the actual value of active power recovery of the wind power generation; and ΔP_{dr} is the active power difference of the demand-side response disconnected with power system during grid fault.

The active power of the demand-side response recovery under post-fault condition applies a conventional control strategy, and the active power difference of the demand-side response is zero. Therefore, the maximum active power difference of power system is:

$$\Delta P_{E1} = \Delta P_{W0} \tag{26}$$

When the proposed power-balancing coordinated control strategy is adopted, there are two different situations. If P_{max} is larger than ΔP_{W0}, the active power matching degree of wind power generation and the demand-side response load is very high. The maximum active power difference of power system will decrease to a very small value, which is given by (27). If P_{max} is ΔP_{W0}, the maximum active power difference of power system is determined by the controllable active power of the demand-side response, which is given by (28). Therefore, the proposed power-balancing coordinated control strategy can significantly improve the frequency stability of power system by reducing the active power shortage under post-fault condition.

$$\Delta P_{E2} = \frac{\Delta P_{W0}}{n} \tag{27}$$

$$\Delta P_{E3} = \Delta P_{W0} - P_{max} \tag{28}$$

V. Simulation Results

To verify the proposed power-balancing coordinated control strategy of the wind power generation and the demand-side response in the paper, the simulation study is carried out on the platform DIgSILENT/PowerFactory. Figure 7 shows the structure of the simulated power grid.

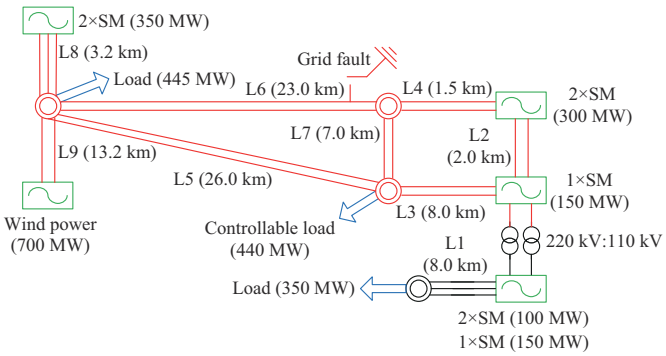

Fig. 7. Structure of simulated power system.

In the simulation, the installed capacity of the thermal power is about 1800 MW and the installed capacity of wind power is about 700 MW. Meanwhile, the installed capacity of fixed load is about 805 MW, which is represented by the constant power load. The maximum power provision of the demand-side response is about 440 MW. The synchronous machine (SM) contains the excitation system, the prime mover, and the speed control system models. All the parameters adopt the actual operating values in the simulation study.

In the simulation, three-phase short-circuit fault arises at 1.0 s with the duration time of 120 ms. For the sake of clarity, two study cases are investigated on the frequency stability of the power system with high-penetration wind power generation. The steady-state active power of the wind power generation is 350 MW in Case 1, and the steady-state active power of the wind power generation is 700 MW in Case 2. Figure 8 presents the active power recovery of the wind power generation under post-fault condition. For convenience of comparison, three control schemes are employed in the simulation tests. In scheme 1, the conventional FRT control strategy of the wind power generation is adopted. The demand-side response loads are uncontrollable, and the active power of the demand-side response recovers quickly under post-fault condition. In scheme 2, the conventional FRT control strategy of the wind power generation is adopted considering that the frequency difference is the largest during the first cycle of frequency fluctuations, and the demand-side response loads can be controlled at the same time. And all the demand-side responses are enabled and switched to the power grid after the first cycle of frequency fluctuations. In scheme 3, the proposed power-balancing coordinated control of the wind power generation and the demand-side response are employed, where the demand-side response switches to the power grid by 10 groups based on the active power recovery of the wind power generation. The active power recovery time is 3.5 s in Case 1 and 8 s in Case 2.

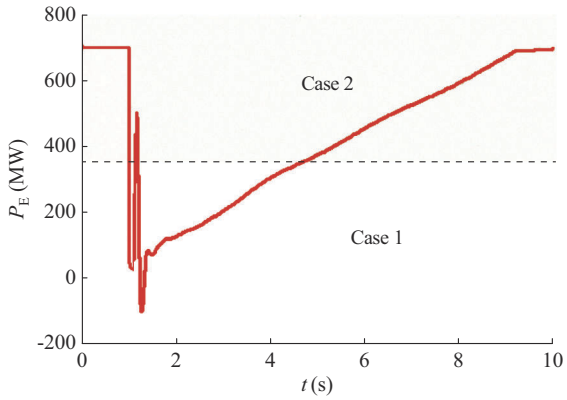

Fig. 8. Active power recovery of wind power generation.

Figure 9 presents the simulation results of the low power provision of the wind power, i.e., Case 1. In this case, the initial active power of the wind power generation is set to be 350 MW under the pre-fault condition. The active power recovers after 3.5 s. P_{max} (440 MW) is larger than ΔP_{W0} (350 MW). At the demand side, the power provision of group 1 is set to be 125 MW and those of the other groups are set to be 35 MW. The time interval of each group switched to power grid is 0.35 s with the proposed power-balancing coordinated control. As can be observed from Fig. 9, the aforementioned three control schemes have little impacts on the grid voltage under the low power provision of

wind power. When scheme 1 is adopted, the grid frequency decreases to 48.7 Hz. If scheme 2 is enabled, where all the demand-side responses are switched after the first cycle of frequency fluctuations, the minimum frequency is 49.1 Hz in the second cycle of frequency fluctuations. If scheme 3 is adopted, the minimum grid frequency is 49.6 Hz.

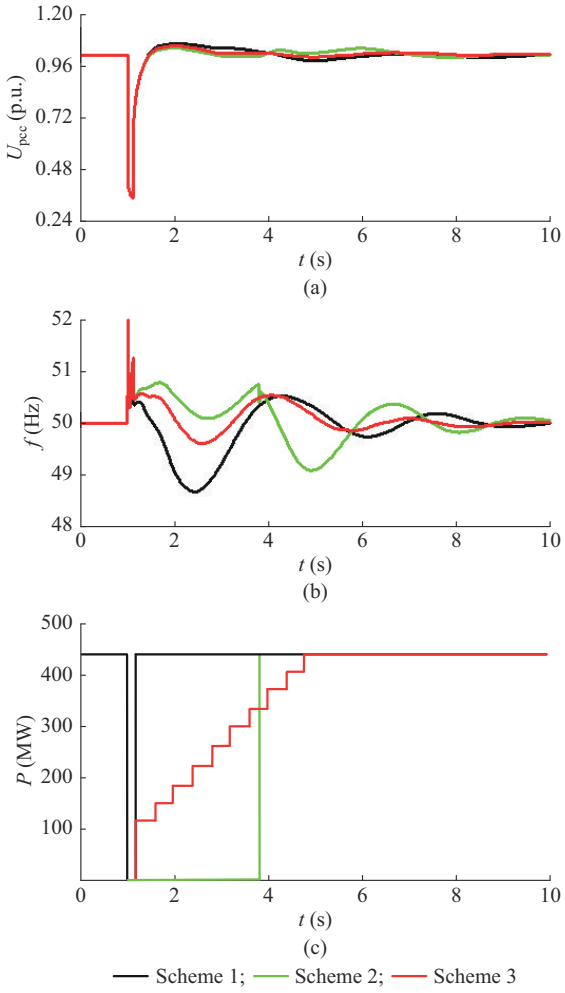

Fig. 9. Simulation results of low wind power provision. (a) Terminal voltage. (b) Grid frequency. (c) Active power of demand-side response.

Figure 10 shows the simulation results of the high power provision of the wind power generation, i.e., Case 2. In this case, the initial active power of the wind power generation is set to be 700 MW under the pre-fault condition. And the active power recovers after 0.8 s. P_{max} (440 MW) is lower than the power difference of the wind power generation ΔP_{W0} (700 MW). At the demand side, the power provision of each group is set to be 44 MW with its maximum power provision. The time interval of each group switching to power grid is 0.8 s with the proposed power-balancing coordinated control. The system frequency decreases to 47.6 Hz if scheme 1 is adopted. If scheme 2 is adopted, all the demand-side responses are switched to the power grid, and the minimum grid frequency is 49.1 Hz in the first cycle of frequency fluctuations. Furthermore, there is a second frequency drop to 48.6 Hz. If scheme 3 is adopted, the grid frequency decreases to 49.0 Hz, which is a litter lower than the grid frequency in Fig. 9. This is mainly because the demand-side response cannot fully compensate the power shortage in the high power provision.

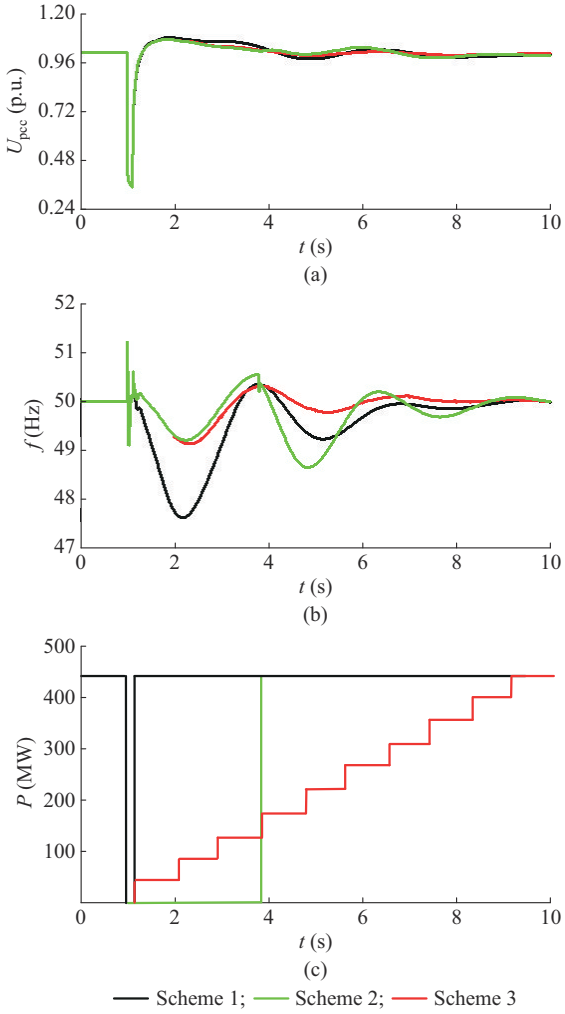

Fig. 10. Simulation results of high wind power provision. (a) Terminal voltage. (b) Grid frequency. (c) Active power of demand-side response.

In summary, the larger impacts of the control strategies on the frequency stability rise with the higher wind power provision. By the means of applying the power-balancing coordinated control of the wind power generation and the demand-side response, the frequency stability can be enhanced with a reduced frequency deviation.

VI. Conclusion

This paper analyzes the frequency performance of the power system with high-penetration wind power generation under post-fault condition, and reveals the impact of frequency disturbance on the control accuracy and the operation stability of wind turbines. Meanwhile, an optimization FRT strategy based on power-balancing is proposed. The following conclusions can be obtained.

1) Due to the FRT control, the wind power has a slow active power recovery under post-fault condition, which would lead to the serious power imbalance in a duration of several seconds with an obvious frequency deviation. Meanwhile, the fre-

quency deviation would also make negative impacts on the accuracy of PLL and control stability of wind power generators.

2) In order to deal with this issue, considering flexible controllability of the demand-side response, the power-balancing coordinated control of the wind power and the demand-side response is proposed. Based on the active power recovery of wind power generation and the maximum controllable active power of the demand-side response, the proposed power-balancing coordinated control can regulate the demand-side response with the flexible power provision.

3) By the proposed power-balancing coordinated control, the theoretical analysis and simulation results are presented to validate that the power imbalance in the power grid can be greatly mitigated under post-fault condition with enhanced frequency stability.

REFERENCES

[1] C. Syranidou, J. Linssen, D. Stolten *et al*., "Integration of large-scale variable renewable energy sources into the future European power system: on the curtailment challenge," *Energies*, vol. 13, no. 20, pp. 1-23, Oct. 2020.

[2] X. Yuan, S. Chen, and J. Hu, "Multi-time scale voltage and power angle dynamics in power electronics dominated large power systems," *Proceeding of the CSEE*, vol. 36, no. 19, pp. 5145-5154, Sept. 2016.

[3] International Renewable Energy Agency (IRENA). Renewable Capacity statistics 2020. (2020, Feb.). [Online]. Available: https://www.irena.org/publications/2020/Mar/Renewable-Capacity-Statistics-2020

[4] X. Qin, L. Su, Y. Chi *et al*., "Functional orientation discrimination of inertia support and primary frequency regulation of virtual synchronous generator in large power grid," *Automation of Electric Power Systems*, vol. 42, no. 9, pp. 36-43, May 2018.

[5] R. Almeida and J. Lopes, "Participation of doubly fed induction wind generators in system frequency regulation," *IEEE Transactions on Power Systems*, vol. 22, no. 3, pp. 944-950, Jul. 2007.

[6] Technical Report on the Events of 9 August 2019. (2019, Sept.). [Online]. Available: https://www. nationalgrideso. com/ document/152346/download

[7] J. Cheng, J. Wang, Y. Huang *et al*., "An orderly charging/discharging control strategy for electric vehicles based on customer's demand in residential area," *Renewable Energy Resource*, vol. 37, no. 11, pp. 1637-1642, Nov. 2019.

[8] K. Clement-Nyns, E. Haesen, and J. Driesen, "The impact of charging plug-in hybrid electric vehicles on a residential distribution grid," *IEEE Transactions on Power Systems*, vol. 25, no. 1, pp. 371-380, Dec. 2010.

[9] Z. Chen, Y. Sun, X. An *et al*., "Integrated demand response characteristics of industrial park: a review," *Journal of Modern Power Systems and Clean Energy*, vol. 8, no. 1, pp. 15-26, Jan. 2020.

[10] H. Zeng, F. Sun, T. Li *et al*., "Analysis of "9·28" blackout in South Australia and its enlightenment to China," *Automation of Electric Power Systems*, vol. 41, no. 13, pp. 1-6, Jul. 2017.

[11] N. Wang, Y. Ma, K. Ding *et al*., "Analysis on root reasons of WTGS nuisance tripping in Jiuquan wind power base," *Automation of Electric Power Systems*, vol. 36, no. 19, pp. 42-46, Oct. 2012.

[12] D. Kaushik, F. Guo, N. Edgar *et al*., "Frequency stability of power system with large share of wind power under storm conditions," *Journal of Modern Power Systems and Clean Energy*, vol. 8, no. 2, pp. 219-228, Mar. 2020.

[13] Q. Shi, G. Wang, W. Ma *et al*., "An experimental study method of D-PMSG with virtual inertia control," *Proceedings of the CSEE*, vol. 35, no. 8, pp. 2033-2042, Apr. 2015.

[14] T. Kerdphol, F. Rahman, M. Watanabe *et al*., "Robust virtual inertia control of a low inertia microgrid considering frequency measurement effects," *IEEE Access*, vol. 7, no. 7, pp. 57550-57560, Apr. 2019.

[15] X. Tian, W. Wang, Y. Chi *et al*., "Virtual inertia optimisation control of DFIG and assessment of equivalent inertia time constant of power grid," *IET Renewable Power Generation*, vol. 12, no. 15, pp. 1733-1740, Aug. 2018.

[16] P. Moutis, "Discussion on primary frequency regulation by deloaded wind turbines using variable droop," *IEEE Transactions on Power Systems*, vol. 29, no. 1, pp. 414-414, Jan. 2014.

[17] J. Liu, Q. Yao, Y. Liu *et al*., "Wind farm primary frequency control strategy based on wind & thermal power joint control," *Proceedings of the CSEE*, vol. 37, no. 12, pp. 3462-3469, Jun. 2017.

[18] J. Yang, J. Zhao, F. Wen *et al*., "Development of bidding strategies for virtual power plants considering uncertain outputs from plug-in electric vehicles and wind generators," *Automation of Electric Power Systems*, vol. 38, no. 13, pp. 92-102, Jul. 2014.

[19] A. Tang, Y. Shao, Q. Xu *et al*., "Multi-objective coordination control of distributed power flow controller," *CSEE Journal of Power and Energy Systems*, vol. 5, no. 3, pp. 348-354, Sept. 2019.

[20] W. Chen, D. Xu, N. Zhu *et al*., "Control of doubly-fed induction generator to ride-through recurring grid faults," *IEEE Transactions on Power Electronics*, vol. 31, no. 7, pp. 4831-4846, Jul. 2016.

[21] M. J. Hossain, T. K. Saha, N. Mithulananthan *et al*., "Control strategies for augmenting LVRT capability of DFIGs in interconnected power systems," *IEEE Transactions on Industrial Electronics*, vol. 60, no. 6, pp. 2510-2522, Jun. 2013.

[22] M. A. Chowdhury, A. Sayem, W. Shen *et al*., "Robust active disturbance rejection controller design to improve low-voltage ride-through capability of doubly fed induction generator wind farms," *IET Renewable Power Generation*, vol. 9, no. 8, pp. 961-969, Jul. 2015.

[23] J. Ouyang, L. Wang, X. Xiong *et al*., "Characteristics and mechanism of short-circuit currents contributed by doubly-fed wind turbines under parallel operation," *Automation of Electric Power Systems*, vol. 40, no. 3, pp. 74-80, Feb. 2016.

[24] M. A. Chowdhury, W. Shen, N. Hosseinzadeh *et al*., "Transient stability of power system integrated with doubly fed induction generator wind farms," *IET Renewable Power Generation*, vol. 9, no. 2, pp. 184-194, Mar. 2015.

Xinshou Tian received the B.E. degree from Huazhong University of Science and Technology, Wuhan, China, in 2008, the M.E. degree from China Electric Power Research Institute, Beijing, China, in 2011, and the Ph.D. degree in electrical engineering from North China Electricity Power University, Beijing, China, in 2016. He is currently an Associate Professor in the Department of China Institute of Energy and Transport Integration Development, North China Electric Power University. His research interests include wind power generation and power system stability analysis.

Yongning Chi received the B.E. and M.E. degrees from Shandong University, Jinan, China, in 1995 and 2002, respectively, and the Ph.D. degree in electrical engineering from China Electric Power Research Institute, Beijing, China, in 2006. Since 2003, he has been employed at China Electric Power Research Institute, Beijing, China, where he is the Chief Engineer for Renewable Energy Department. His research interests include modeling, control and integration analysis of renewable energy generation.

Chao Liu received the B.S. degree from Shandong University, Jinan, China, in 2006, and the M.S. degree from Shandong University in 2009. Since 2009, he has been employed at China Electric Power Research Institute as Renewable Energy Integration Planning and Simulation Research Division Director of Renewable Energy Department. His research interests include power system analysis, renewable energy modeling and grid integration simulation, renewable energy development planning.

Peng Cheng received the B.S. and Ph.D. degrees both in electrical engineering from Zhejiang University, Hangzhou, China, in 2011 and 2016, respectively. He is currently an Assistant Professor in the Department of China Institute of Energy and Transport Integration Development, North China Electric Power University, Beijing, China. His research interests include multi-converter power systems and renewable power generation, especially wind power generation.

Yan Li received the B.S. degree from Shandong University of Technology, Zibo, China, in 1999, the M.S. degree from Fuzhou University, Fuzhou, China, in 2002, and the Ph.D. degree from China Electric Power Research Institute, Beijing, China, in 2007. Since 2007, he has been employed at China Electric Power Research Institute as Renewable Energy Integration Planning and Simulation Research Division Director of Renewable Energy Department. His research interests include power system analysis, renewable energy modeling and grid integration simulation, and renewable energy develoepement planning.